Sensors **2007**, *7*, 860-883

sensors
ISSN 1424-8220

www.mdpi.org/sensors

Full Research Paper

Comparison of Three Operative Models for Estimating the Surface Water Deficit using ASTER Reflective and Thermal Data

Mónica García [1,*], Luis Villagarcía [2], Sergio Contreras [1], Francisco Domingo [1,3] and Juan Puigdefábregas [1]

[1] Departamento de Desertificación y Geoecología. Estación Experimental de Zonas Áridas. General Segura, 1. 04001, Almería, Spain. Phone: +34-950281045, Fax: +34 950 27 71 00. monica@eeza.csic.es, sergio@eeza.csic.es, poveda@eeza.csic.es, puigdefa@eeza.csic.es
[2] Departamento de Sistemas Físicos, Químicos y Naturales. Universidad Pablo Olavide. Sevilla. Spain lvisail@upo.es
[3] Departamento de Biología Vegetal y Ecología, Escuela Politécnica Superior, Universidad de Almería, 04120 Almería, Spain

* Author to whom correspondence should be addressed.

Received: 5 April 2007 / Accepted: 4 June 2007 / Published: 6 June 2007

Abstract: Three operative models with minimum input data requirements for estimating the partition of available surface energy into sensible and latent heat flux using ASTER data have been evaluated in a semiarid area in SE Spain. The non-evaporative fraction (NEF) is proposed as an indicator of the surface water deficit. The best results were achieved with NEF estimated using the "Simplified relationship" for unstable conditions (NEF_{Seguin}) and with the S-SEBI (Simplified Surface Energy Balance Index) model corrected for atmospheric conditions ($NEF_{S\text{-}SEBIt,}$) which both produced equivalent results. However, results with a third model, $NEF_{Carlson}$, that estimates the exchange coefficient for sensible heat transfer from NDVI, were unrealistic for sites with scarce vegetation cover. These results are very promising for an operative monitoring of the surface water deficit, as validation with field data shows reasonable errors, within those reported in the literature (RMSE were 0.18 and 0.11 for the NEF, and 29.12 Wm^{-2} and 25.97 Wm^{-2} for sensible heat flux, with the Seguin and S-SEBIt models, respectively).

Keywords: ASTER, evapotranspiration, surface energy balance, semiarid.

1. Introduction

The relationship between ecosystem latent heat (λE) and sensible heat (H) flux is critical to quantify the surface water deficit and to understand the hydrological cycle. The law of conservation of energy states that the available energy reaching a surface is dissipated as latent heat (λE) and/or sensible heat (H), the partition of which depends mostly on water availability. Factors affecting this relationship include longer-term interactions between biogeochemical cycles, disturbances and climate, and shorter-term interactions between plant physiology and the development of the atmospheric boundary layer [1].

Remote sensing is currently the only source of data providing frequent and spatially disaggregated estimates of radiometric temperature, albedo and surrogates of vegetation cover, variables that explain most of the partition of the available energy into H and λE. Therefore, model development using inputs from remote sensing data in the solar and thermal domain is a very active subject of research [2]. Still, there is always a trade-off between model parameterization requirements and operativity that has to be carefully evaluated in each case when selecting a methodology.

A widely used water deficit indicator is the evaporative fraction: EF=λE/(H+λE) [3, 4]. However, in semiarid areas, λE and therefore the evaporative fraction (EF) of natural vegetation are very low during several days, with values sometimes lower than the accuracy levels of remote sensing models for estimating evapotranspiration (<1 mm for λE) [2, 5].

We, therefore, propose using the non-evaporative (NEF) fraction to evaluate the surface water deficit, defined as:

$$NEF = 1 - EF = 1 - \frac{\lambda E}{\lambda E + H} = 1 - \frac{\lambda E}{Rn - G} = \frac{H}{Rn - G} \quad (1)$$

where Rn = net radiation; G = soil heat flux; and Rn-G = available energy.

In semiarid areas, the NEF should have a wider range of variability than the EF and a higher SNR (signal-to-noise ratio). It can be observed that the NEF is directly related to the Bowen ratio (β=H/λE). Introducing Equation (1) in the Bowen ratio gives Equation (2):

$$\beta = \frac{NEF}{1 - NEF} \quad (2)$$

The NEF is also similar to the Water Deficit Index (WDI) of [6] in which WDI=1-Ea/Eo, where Ea is actual evapotranspiration and Eo is potential evapotranspiration, using available energy for evapotranspiration (Rn-G) instead of the potential evapotranspiration, and latent heat (λE) which is equivalent to Ea.

The purpose of this study is to evaluate three simple operative models with minimum input data requirements for estimating the non-evaporative fraction (NEF) in southeast Spain. Two of the models are based on the "Simplified Relationship", estimating daily H and Rn [7] with two parameterizations for H, [8] and [9]. The third model is based on the S-SEBI (Simplified Surface Energy Balance Index) [4], which estimates the evaporative fraction (EF) directly from the relationship between albedo and surface temperature, modified for this study to account for atmospheric conditions.

The study site, located in Almería (Spain) in the Mediterranean Basin, is characterized by escalating water demands for agriculture and tourism, leading to overexploitation of groundwater resources [10]. Given the strategic importance of recharge processes in the region's environmental and socio-economic system, it is crucial to have more information about the spatial partition of surface energy.

ASTER (Advanced Spaceborne Thermal Emission and Reflection Radiometer) data were used to calculate the non-evaporative fraction (NEF). ASTER is currently the only sensor collecting multispectral thermal infrared data at high spatial resolution, being very appropriate for model testing and direct ground comparison [11]. Furthermore, ASTER is on the Terra platform along with the MODIS sensor (Moderate Resolution Imaging Spectroradiometer), making it possible to scale up analyses from field to regional or global scales [12].

2. Description of the study region and data acquired

2.1. Study region

The study region (Figure 1), located in the south-eastern Iberian Peninsula (Almería, Spain), comprises 3600 km^2 (36.95ºN, 2.58ºW). It is characterized by its heterogeneity, with altitudinal gradients ranging from sea level up to 2800 m (a.s.l.) in the Sierra Nevada Mountains. Precipitation and temperature regimes vary widely due to the orography [13]. Annual precipitation is the lowest in Tabernas lowlands, where it is less than 200 mm, while in the mountains it ranges from 400 mm to 700 mm, enough to sustain forest growth.

In the center of the study site, the karstic landscape of the Sierra de Gádor mountain range, covering 552 km^2, consists of a series of thick carbonate rocks (limestones and dolomites), highly permeable and fractured with intercalated calcschists of low permeability underlain by impermeable metapelites [10]. The southern edge of this mountain range is the main source of recharge for the deep Triassic aquifers of the Campo de Dalías [10]. In general, the soils are very thin, rocky and very vulnerable to flash flooding and erosion, the most representative type being Lithic-Typic Haploxeroll according to the FAO classification [14]. The Sierra de Gádor mountains underwent intense, widespread deforestation during the 18^{th} and 19^{th} centuries, when the original oaks (*Quercus ilex* L. and *Quercus faginea* Lam.), olive trees (*Olea europaea* L.), poplars (*Populus* L. spp.) and strawberry-trees (*Arbutus unedo* Lam.) were cut down for ship construction, fuel and wood for mining activities. Other current pressures or disturbances in the Sierra de Gádor include construction, fire, agriculture and sheep grazing. Nowadays the area is dominated by a sparse shrubland, mostly *Genista cinerea* Vill, with rock outcrops, bare soil or some grasslands mainly composed of *Festuca scariosa* Lag. Around 73% of Sierra de Gádor presents this pattern with vegetation cover lower than the 50%.

Shrubland with a sparse cover of pine woodland (*Pinus L. spp*.) is the second largest natural land cover type (12% of the area). Only 1.5% of the land is covered by dense pine reforestation. 9% of the Sierra de Gádor is dedicated to agriculture (almond and olive trees) [15].

The rest of the study site includes part of the Sierra Nevada Natural Park, composed of pine forest with oak relicts and shrublands. To the northeast, there is the Tabernas Lowlands, an area of badlands with complex topography. Along the ephemeral Andarax River, which flows past the capital city of Almeria, there is a mosaic of citrus orchards and vineyards. One of the most salient features of the scene is the large area of plastic greenhouses spreading over more than 330 km^2. This unique

combination of land covers and uses makes this area an ideal pilot site for model testing. Two field research stations acquire data continuously in the study region, *Llano de los Juanes* in the Sierra de Gádor and *Rambla Honda* in the Tabernas Lowlands, shown by white arrows in Figure 1.

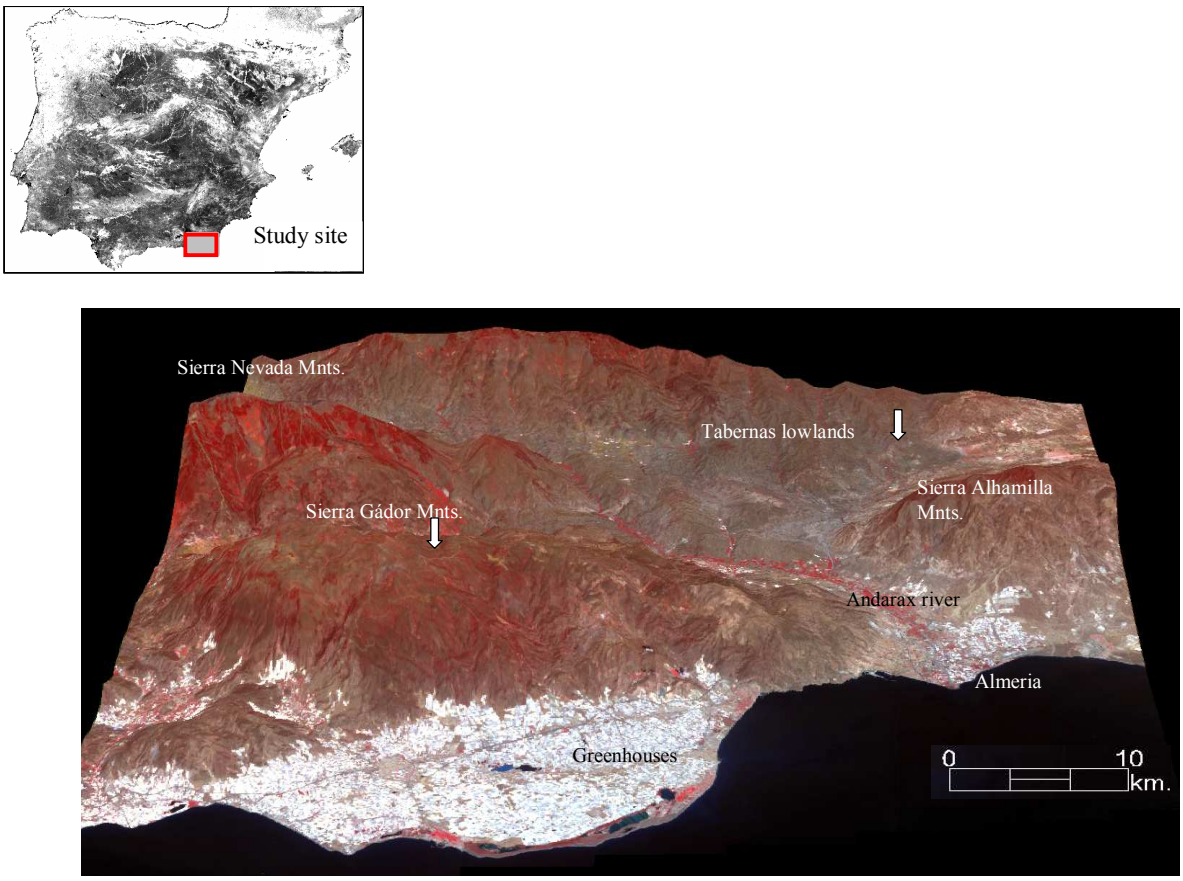

Figure 1. Study site in southeast Spain (Almería). The large image shows a 3D surface with elevation, and ASTER RGB false-color composite (15 m) taken on July 18, 2004. Three mountain ranges are visible: part of the Sierra Nevada, part of the Sierra Alhamilla and the Sierra de Gádor. White arrows show the location of the two research sites: *Llano de los Juanes* in the Sierra de Gádor and *Rambla Honda* in the Tabernas Lowlands.

2.2. Field research sites in the study region

Llano de los Juanes research site

Instrumental field data have been acquired continuously at the *Llano de los Juanes* research site since September 2003 (Figure 1). Latent and sensible heat flux are measured by an eddy covariance system using a three dimensional sonic anemometer CSTAT3 and a krypton hygrometer KH_20 (both from Campbell Scientific Inc., USA). *Llano de los Juanes* is a representative ~2 km^2 flat area located at an altitude of 1600 m in the high, well-developed karstic plain of the Sierra de Gádor. Fetch is sufficient for the vegetation height and sensors. Vegetation cover is 50-60% and consists mainly of patchy perennial dwarf shrubs (30-35%) dominated by *Genista pumilla*, *Thymus serpylloides* Bory and *Hormathopylla spinosa* L., and grasses (20-25%) dominated by *Festuca scariosa* Lag. and

Brachypodium retusum Pers. [16]. Mean NDVI measured in *Llano de los Juanes* with a Dycam camera in June 2004 was 0.30.

Net radiation (NR-LITE; Kipp & Zonen, Delft, Netherlands), relative humidity (thermohygrometer HMP 35C, Campbell Scientific, Logan, UT, USA), soil temperature (SBIB sensors) and soil heat flux (HFT-3, REBS, Seattle, WA, USA) have also been continuously measured at the site since September 2003. Annual precipitation recorded during the last three hydrological years by a rain gauge mounted in 2003 varied considerably: 506.7 mm in 2003/04, 212.4 mm in 2004/05, and 328.1 mm in 2005/06.

Rambla Honda research site

The *Rambla Honda* research site is located in a dry valley near Tabernas, Almería, Spain (37º8'N, 2º22'W, 630 m altitude). For a detailed description of the site, see [17]. The valley has been abandoned for several decades and the only activity is now restricted to small-scale sheepherding.

Three perennial species dominate the landscape, *Retama sphaerocarpa* (L.) Boiss shrubs across the valley floor, *Stipa tenacissima* L. tussocks on the steep sides of the valley and *Anthyllis cytisoides* L. shrubs on alluvial fans between the two. The valley floor has deep loamy soils overlying mica schist bedrock. The average annual rainfall is 220 mm with a dry season from June to September.

Experiments related to hydrology and erosion [18, 19], surface energy balance and evapotranspiration [5, 20-25] and vegetation ecology [26-28] among others have been performed at the site during the last decade.

The eddy covariance system, currently located at *Llano de los Juanes*, was acquiring data in *Rambla Honda* between February 2002 until July 2003. Evapotranspiration was also measured by the BREB (Bowen Ratio Energy Balance) and transpiration with sap flow measurements. This allowed a detailed SVAT (Soil-Vegetation-Atmosphere Transfer) model to be calibrated for *Retama sphaerocarpa* with a 10% error in daily evapotranspiration compared to the BREB. This SVAT model [20] is an extension of [29] model which combined the [30] and [31] approaches to account for energy partition in sparse vegetation by explicitly separating contributions from soil and vegetation. The parameterization was further extended to the other two dominant species in the area, *Anthyllis cytisoides*, and *Stipa tenacissima* with errors (as % of the mean±std) of 5.6±1.8 and 7.3±0.07, respectively, compared to the BREB. Therefore, in the three species, errors were within the uncertainty of the validation system. Because model calibration was performed for a time span representative of the variability encountered in surface and climate variables at longer time scales, the model can now be run, as the input variables required for parameterization are still being acquired at the site.

The variables used for this study include net radiation (NR-LITE; Kipp & Zonen, Delft, Netherlands), relative humidity (thermohygrometer HMP 35C, Campbell Scientific, Logan, UT, USA) sonic and soil temperature (SBIB sensors), wind speed, and soil heat flux.

2.3. Remote sensing and spatial data

ASTER (Advanced Spaceborne Thermal Emission and Reflection Radiometer) data on July 18, 2004, July 9, 2004 and June 19, 2005 at 11.00 UTC were acquired for this study. ASTER is an imaging instrument on-board of Terra, a satellite launched in December 1999 as part of the NASA's Earth Observing System (EOS). ASTER is a cooperative effort between NASA, Japan's Ministry of Economy, Trade and Industry (METI) and its Earth Remote Sensing Data Analysis Center (ERSDAC)

[32]. ASTER scans a swath of 60 km on the ground every 16 days with a swath angle of ±2.4. The sensor has nine reflective bands and five bands in the thermal infrared (TIR) region.

The ASTER products used in our research included surface reflectance (2AST07) with a spatial resolution of 15 m (VNIR) and 30 m (SWIR), and kinetic temperature at 90 m (2AST0) with a surface temperature absolute precision of 1-4 K. No incidences have been reported for these scenes. The three images did not cover exactly the same area due to ASTER's off-nadir sensor pointing capability.

A digital elevation model (DEM) from the USGS (United States Geological Survey) with a 30 m resolution and a digital 0.5-m pixel orthophoto (from the Andalusian Regional Government) were used at different stages of the study.

Half-hourly air temperatures (ºC) at the time of the satellite overpass (11.00 UTC) were acquired from meteorological stations for validation purposes. Ten or eleven stations were available for each image depending on scene coverage. Seven of the stations belong to the EEZA (Estación Experimental de Zonas Áridas), and the rest to the Andalusian Regional Government, (Red de Información Agroclimática de Andalucía).

3. Methodology for estimating the non-evaporative fraction (NEF)

3.1. Estimating the non-evaporative fraction from the "Simplified Relationship"

Daily NEF (non-evaporative fraction) was estimated from ASTER and ancillary data using the ratio between daily sensible heat (H) and net radiation (Rn): H/Rnd.

Soil heat flux (G) can be considered negligible at a daily scale compared to the other components of the surface energy balance [2, 8], as shown in Equation (3):

$$NEF = 1 - EF = 1 - \frac{\lambda E}{\lambda E + H} = 1 - \frac{\lambda E}{Rnd - G} = \frac{H}{Rnd - G} \approx \frac{H}{Rn} \quad (3)$$

where EF is the evaporative fraction, λE is latent heat flux (Wm^{-2}), H is the sensible heat flux (Wm^{-2}) and Rnd is the daily net radiation (Wm^{-2}).

Daily net radiation (Rnd)

Daily net radiation (Rnd) was calculated as the balance between incoming (↓) and outgoing fluxes (↑) of shortwave (Rs) and longwave (Rl) radiation. By agreement, incoming fluxes are positive and outgoing negative. Net radiation is the sum of net shortwave (Rns) and net longwave radiation (Rnl) [2].

First, Rni, instantaneous net radiation at the time of image acquisition, was calculated by estimating its four components:

$$Rni = Rs\uparrow + Rs\downarrow + Rl\uparrow + Rl\downarrow = Rns + Rnl \quad (Wm^{-2}) \quad (4)$$

The shortwave net radiation using remote sensing data was calculated as in Equation (5):

$$Rns = Rs\downarrow (1 - \alpha) \quad (Wm^{-2}) \quad (5)$$

Rs↓ is the incoming solar radiation or incoming shortwave radiation, which was estimated at the time of the satellite overpass (11.00 UTC) using a solar radiation model [33] accounting for elevation, aspect, latitude and longitude, solar geometry, atmospheric transmissivity, and the influence of the surrounding topography. α is the broadband surface albedo estimated according to [34] as follows:

$$\alpha = \rho_1 \cdot 0.484 + \rho_3 \cdot 0.335 - 0.324 \cdot \rho_5 + 0.551 \cdot \rho_6 + 0.305 \cdot \rho_8 - 0.367 \cdot \rho_9 - 0.0015 \quad (6)$$

Where ρ_i is reflectance at the surface for the band indicated by the subscript i. Reflectance was acquired from ASTER product 2AST07.

The longwave energy components are related to surface and atmospheric temperatures by the Stefan-Boltzmann Law. The outgoing longwave radiation was calculated at the time of image acquisition as in Equation (7):

$$Rl\uparrow = -\varepsilon_s \sigma T_s^4 \quad (Wm^{-2}) \quad (7)$$

Where σ is the Stefan-Boltzmann constant, (5.67×10^{-8} W m^{-2}), T_s is surface temperature (K), and ε_s is broadband emissivity for the surface, estimated based on the logarithmic relationship to NDVI as proposed by [35]:

$$\varepsilon_s = 1.0094 + 0.047 \cdot \mathrm{Ln}(NDVI) \quad (8)$$

Radiometric surface temperature, T_s, was acquired directly from the ASTER kinetic temperature product retrieved by the TES (Temperature Emissivity Separation) algorithm.

An empirical function was used for the incoming longwave radiation Rl↓ [36].

$$Rl\downarrow = (1-\varepsilon_s) \cdot \sigma T_s^4 \left(1 - c^{\left(-d(Tair-273)^2\right)}\right) \quad (Wm^{-2}) \quad (9)$$

where T_{air} is the air temperature and c and d are constants (0.261 and $7.77\ 10^{-4}$ K^2, respectively).

Daily net radiation (Rnd) (Wm^{-2}) was calculated from Rni by assuming Rnd/Rni≈0.3 ±0.03 at midday as proposed by [8].

Sensible heat flux (H)

The sensible heat flux (H) can be estimated by the turbulent transport from the surface to the lower atmosphere based on surface layer similarity of mean temperature and wind speed profiles using the resistance formula:

$$H = \rho \cdot C_p \frac{T_s - T_{air}}{r_h} \quad (Wm^{-2}) \quad (10)$$

where Ts is the land surface temperature and Tair is the air temperature, both at the time of image acquisition; r_h is a turbulent exchange coefficient dependent on wind speed, aerodynamic roughness length, roughness length for heat transfer and Monin-Obukov length [37] , and ρ and Cp are air density and specific heat at constant pressure, respectively. Due to differences between radiometric surface temperature and aerodynamic surface temperature, another resistance term Kb^{-1} (excess resistance) was added to the denominator of Equation (10) to account for the difference between roughness length for heat (z_o) and momentum (z_{oh}): $Kb^{-1}=\ln(z_o/z_{oh})$. However, in practice, it is hard to get large-scale

spatial estimates for all the variables in the resistance terms of H, therefore more operational parameterizations have been proposed.

One of the most widely used approaches to solving the surface energy balance that explicitly calculates H and Rnd is the so-called "Simplified Relationship" [7, 8, 38] which states that daily evapotranspiration (λE_d) can be estimated from the difference between daily net radiation (Rnd) and daily sensible heat flux (H), by estimating H from the difference between instantaneous surface (Ts) and air temperatures (T_{air}) near midday, as in Equation (11):

$$H = B \cdot (T_s - T_{air)ins\ tan\ t} \quad (mm\ day^{-1}) \tag{11}$$

The "Simplified Relationship" has been verified empirically and theoretically [8,39-41]. B can be defined as a mean exchange coefficient of sensible heat transfer. According to this relationship, the surface-atmosphere temperature gradient at midday, related to the instantaneous sensible heat flux at midday by means of B, can be considered representative of the influence of daily H in the energy balance by assuming that the evaporative fraction is constant throughout the day [3,8,42]. Considering this and equation (10), B could be estimated as in (12):

$$B \approx (R_{nd} / R_{ni}) \frac{\rho \cdot Cp}{rh} \quad (mm\ K^{-1} day^{-1}) \tag{12}$$

[8] proposed two values for B as a first approximation, 0.25 $mmK^{-1}day^{-1}$ for stable atmospheric conditions (T_s - T_a<0) and 0.18 $mmK^{-1}day^{-1}$ for unstable conditions (T_s - T_{air} > 0). At our study site at the time of image acquisition, unstable conditions tend to be prevalent [20].

Another operative approach for estimating H that also builds upon the simplified relationship was proposed by [9]. They showed that the main factor affecting resistance to heat transfer, and therefore B, was vegetation cover, and established a linear relationship between fractional cover and B, and between fractional cover and an exponent n close to 1 affecting the (T_s-T_{air}) term. To estimate fractional cover NDVI was rescaled between values associated with sites where fractional cover is 0 (bare soil sites) and sites with vegetation cover =1, associated with dense forest sites. In our study site NDVI from associated to those two extremes was: 0.16 ± 0.012 (mean ± standard deviation) for bare soil sites and 0.68 ± 0.20 from complete vegetation cover. Mean values from bare soil and complete vegetation were taken to calculate B and n.

Hereinafter we will refer to NEF and H as calculated using the [8] model for stable conditions as NEF_{Seguin} and H_{Seguin} and the one by [9] as $NEF_{Carlson.}$ and $H_{Carlson.}$

Air temperature (T_{air})

Air temperature (T_{air}) is used to estimate sensible heat flux and net radiation. To avoid relying on meteorological information, T_{air} was estimated from the images using the NDVI-Ts triangle as proposed by [9] in an approach similar to [43] and [43, 44]. The apex of the NDVI-Ts space (high NDVI and low temperature) should correspond to pixels with high NDVI located at the wet edge of the triangle, and can be assumed to be at T_{air}. T_s at the apex is found by locating minimum surface temperature areas in the scene. Those with the highest NDVI corresponding to forest patches are

identified, and the average T_s for that selected region is calculated. Due to the altitudinal gradients in the study region, T_{air} must be corrected using the pixels at the region forming the apex as a reference altitude. Then positive corrections for altitude can be made for pixels below the baseline and vice-versa for pixels above it, considering a lapse rate of 6.5ºC per 1000 m. This works better than considering a single T_{air} for the whole area, by assuming constant meteorological conditions at the blending height [9] or the dry and wet pixel method used by [3], evaluated in preliminary tests (results not shown), and which is probably better suited for flat areas.

3.2. Estimating the non-evaporative fraction from S-SEBI (Simplified-Surface Energy Balance Index)

Another method of estimating the NEF, other than explicitly estimating surface energy balance variables, was derived from the S-SEBI (Simplified Surface Energy Balance Index) [4]. S-SEBI directly estimates the evaporative fraction, EF, on a pixel basis by means of a contextual relationship between surface temperature (T_s) and albedo. It has been applied to estimate the evaporative fraction for crops and natural vegetation at different spatial scales [45-47] and assumes that atmospheric conditions remain relatively constant across the study region, and requires enough wet and dry pixels in the scene for hydrological contrast.

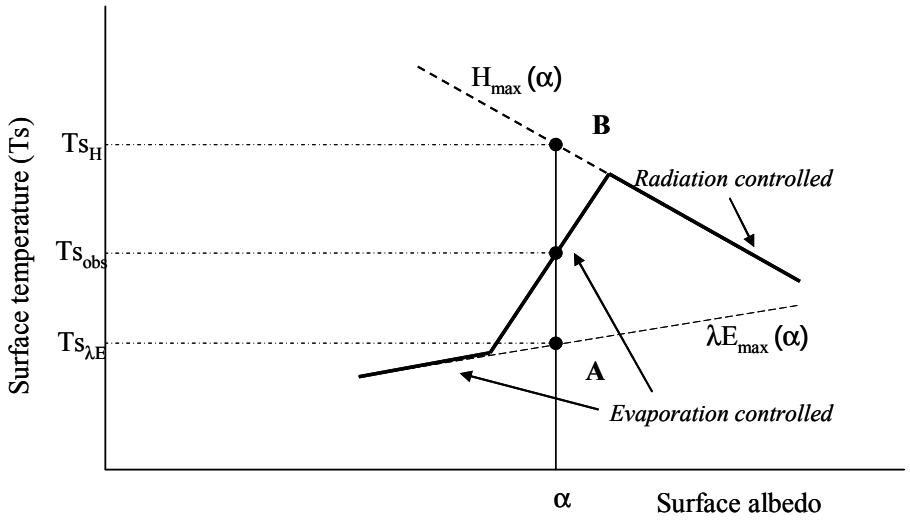

Figure 2. Scheme of the S-SEBI model (adapted from [4]) showing the relationship between surface albedo (α) and surface temperature (Ts). "A" and B" correspond to the evaporation-controlled and radiation-controlled domains, respectively. Ts_{obs} is the observed temperature, $Ts_{\lambda E}$ is the temperature in the evaporation-controlled domain and Ts_H is the temperature in the radiation-controlled domain.

Boundary conditions for the model can be extracted from the scatter plot of Ts and albedo. At low reflectance, Ts is almost constant with increasing albedo (Line "A" in Figure 2). This would be the case of saturated water surfaces or irrigated areas where all available energy is used for evapotranspiration (EF≈1; with maximum evapotranspiration, λE_{max}). When albedo increases, Ts also increases because of reduced evapotranspiration at the expense of increased sensible heat flux. This is also within the "evaporation-controlled domain". When albedo increases beyond a certain level, there

is an inflection point, and Ts begins to decrease with albedo (line "B" in Figure 2). At this point soil moisture is so low that no evaporation can take place and all the available energy is dissipated as sensible heat flux (EF≈0 with maximum sensible heat flux, H_{max}). However, the increase in albedo produces a decrease in shortwave net radiation reducing Ts. This is the "radiation controlled domain". Rescaling each observed Ts according to these boundary conditions, "A" and "B" in Figure 2 allows to obtain EF as expressed in Equation (14):

$$EF = \frac{Ts_{obs} - Ts_{\lambda E}}{Ts_H - Ts_{\lambda E}} \tag{14}$$

where Ts_{obs} is the observed temperature, $Ts_{\lambda E}$ is the temperature at the lower boundary function or the evaporation-controlled domain and Ts_H is the temperature at the upper boundary function or radiation-controlled domain.

We modified the S-SEBI to account for variation in atmospheric conditions across the study site. Therefore, in this study, surface temperature (Ts) was standardized by T_{air} using the following equation to calculate NEF:

$$NEF = 1 - EF = 1 - \frac{DT_{obs} - DT_{\lambda E}}{DT_H - DT_{\lambda E}} \tag{15}$$

Where DT_{obs} is the observed difference between surface and air temperature, $DT_{\lambda E}$ is the difference between surface and air temperature at the lower boundary function or evaporation-controlled domain, and DT_H is the difference between surface and air temperature at the upper boundary function or radiation-controlled domain.

Both the upper and lower boundary functions were calculated by quantile regression [48] from the scatter plot of albedo vs. Ts for the study region, using the 5% and the 95% quantiles, respectively. H was estimated by multiplying NEF by Rnd, assuming daily G to be zero, for comparison with H_{Seguin} and $H_{S\text{-}SEBIt}$.

The NEF and H calculated by this approach, in which the original S-SEBI (Simplified-Surface Energy Balance Index) formulation for calculating the EF (evaporative fraction) was modified by including T_{air}, are hereinafter referred to as $NEF_{S\text{-}SEBIt}$ and $H_{S\text{-}SEBIt}$.

3.3. Validation of the non-evaporative fraction model results

It is extremely complicated to validate surface energy fluxes estimated from remote sensing data due to limitated availability of measured surface fluxes for several surface types over large scales. In addition, field measurements and remote sensing footprints are not always comparable. In this paper we propose two validation procedures (a) Comparison of representative semi-arid vegetation surface types for which these field surface fluxes were available: *Retama, Anthyllis* and *Stipa*, and a mixture of shrubs and forbs (b) Evaluation of NEF estimated at sites of known vegetation and land cover.

The eddy covariance system located at *Llano de los Juanes* research site has been acquiring data over the shrublands, being the fluxes representative of an area of approximately 2 km^2 since Fall 2003. At the *Rambla Honda* research site, outputs from the detailed SVAT model parameterized by [20] and [49] for *Retama, Anthyllis* and *Stipa,* with errors of < 10%, were used as field references. For

comparison between the image and modeled data, patches of those species in *Rambla Honda* were selected based on field visits and the aerial photo (0.5 m). The *Rambla Honda* field site was only present in the July 18th 2004 scene.

In addition, we used the wetland named "Cañada de las Norias" located in the greenhouse area as a validation site. For validation purposes we considered a field value for daily H=0, and therefore also for NEF=0, similarly to [3] and [4]. The wetland comprises 135 ha with a maximum depth of 2 m. The riparian vegetation is composed of *Phragmites australis*, *Tamarix canariensis*, and *Tamarix africana*, the latter also appears within the water table, and in the shallower parts *Typha domingensis* and *Scirpus litoralis*. Within the wetland macroalgi from *Entermorpha* and *Cladophora* genus, indicative of high eutrofization, tend to replace aquatic macrophytes [50]. Solids and algi increase water turbidity and reduce the effective penetration of solar radiation in the water column, which reduces the water storage term at a daily scale (G) [51] that becomes almost negligible in the case of vegetated wetlands [52].

In shallow lakes such as "Cañada de las Norias", heat accumulates during the day and supplies evaporative heat loss at night. Thus, although hourly changes in the storage term (G) can be high, on a daily basis (24 hr) G is smaller. For instance, in a similar wetland of the same area hourly G fits in summer a sinusoidal curve with midday peaks of around 50 Wm^{-2} [51, 53]. In the Daimiel wetlands in Central Spain, daily energy storage (24 hr) on open water presents oscillations of ±39.9 Wm^{-2} [54]. In a semiarid shallow wetland in Nebraska, G for open water ranged between -76 and 60 Wm^{-2} with those extremes associated with rainy or cloudy days [55].

Regarding the sensible heat flux (H) on a daily basis its contribution to the wetland energy balance is minimum. In a semi-arid wetland daily H presented values ranging between ±20 Wm^{-2}. In a wetland nearby "Cañada de las Norias", H contribution to heat budget was found to be less than 2% [53].

Because NEF_{Seguin} and $NEF_{Carlson}$ models assume G=0, which is correct over land surfaces, modeled results over the lake were corrected just for validation considering NEF=H/(Rn-G) instead of NEF=H/Rn by assuming a daily G value in the wetland at the most between ±50 Wm^{-2} (around ±23% of Rn)-.

Estimated means of H, Rnd and NEF from each patch in the image and observed daily means from the eddy covariance or the SVAT model were compared in terms of R^2, RMSE (Root Mean Square Error), MAE (Mean Absolute Error), p, slope and intercept of the linear regression.

4. Results and discussion

4.1. Comparison of models estimating the non-evaporative fraction (NEF)

Spatial patterns with the $NEF_{S\text{-}SEBIt}$ and NEF_{Seguin} were observed to be more similar to each other on the three dates than with the $NEF_{Carlson}$ model, although $NEF_{S\text{-}SEBIt}$ always yielded higher values. Across the study site, the lowest NEF with $NEF_{S\text{-}SEBIt}$ and NEF_{Seguin} corresponded to water surfaces (sea and lakes), and high-altitude mountain forests. The highest NEF were located in the Tabernas lowlands which is plausible at this time of the year. However, $NEF_{Carlson}$ values in the Tabernas lowlands where vegetation cover is scarce, are unrealistically low. Figure 3 shows an example of results for NEF (non-evaporative fraction) on July18, 2004.

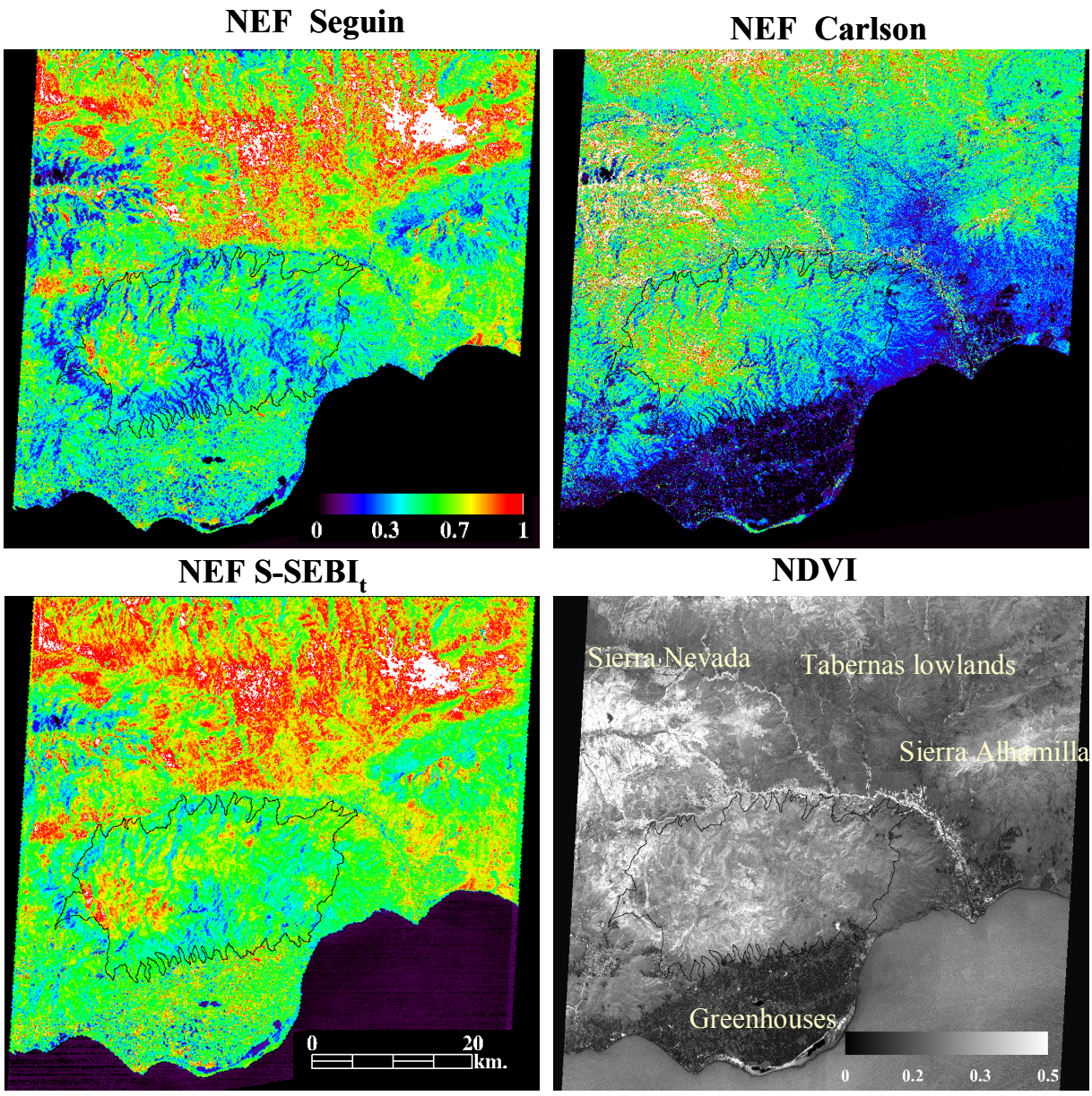

Figure 3. NEF (non-evaporative fraction) using NEF_{Seguin}, $NEF_{Carlson,}$ and $NEFS\text{-}_{SEBIt.}$ models for July 18, 2004. NDVI levels on this date are shown in the grey scale image. The Sierra de Gádor in the center of the study site is outlined in black.

Linear regression of NEF on the three dates using all the pixels in each scene, including sea water, and the greenhouse area, shows (Table 1) very good correspondence between NEF_{Seguin} and $NEF_{S\text{-}SEBIt.}$ but not between $NEF_{Carlson}$ and the other two models.

Table 1. Comparison of NEF (non-evaporative fraction) obtained with NEF_{Seguin}, $NEF_{Carlson}$ and $NEF_{S\text{-}SEBIt}$ models on the three dates using all the pixels in each image. RMSE is the root mean square error and p is the probability level associated with the regression.

NEF models	Date		
	July 7, 2004	**July 18, 2004**	**June 19, 2005**
NEF_{Seguin} vs. $NEF_{S\text{-}SEBIt}$			
R^2	0.97	0.98	0.96
p	0.0000	0.0000	0.0000
RMSE	0.34	0.13	0.18
slope	1.0	0.83	0.94
intercept	0.34	0.18	0.20
NEF_{Seguin} vs. $NEF_{Carlson}$			
R^2	0.51	0.47	0.50
p	0.0000	0.0000	0.0000
RMSE	0.34	0.73	0.21
slope	0.49	0.66	0.84
intercept	0.08	0.05	0.16
$NEF_{Carlson}$ vs. $NEFS_{SEBIt}$			
R^2	0.43	0.46	0.51
p	0.0000	0.0000	0.0000
RMSE	0.45	0.67	0.22
slope	0.24	0.34	0.58
intercept	-0-006	0.59	0.35

When model performance is examined more in detail for certain surface types on each date as a first approach to validating our results (Figure 4), it is observed that the most coherent patterns in NEF are provided by NEF_{Seguin} and $NEF_{S\text{-}SEBIt}$ with a high NEF for dry, bare soil sites and low NEF in mountain forest sites. The $NEF_{Carlson}$ seems reasonable for forest types, with values similar to NEF_{Seguin}. However, over bare soil surfaces, $NEF_{Carlson}$ greatly underestimates NEF yielding even lower levels than forests (e.g., the limestone quarry would be evapotranspiring at the same rate as water according to $NEF_{Carlson}$). The [9] approach has been successfully used in Argentina at sites with NDVI over 0.5 [56], however, in semiarid sites with low NDVI, estimating the B exchange coefficient for sensible heat transfer based solely on NDVI produces unrealistic patterns. It is therefore preferable to consider a constant value of B as at least a first approximation. In the Sierra de Gádor, B does not vary much: 0.24± 0.10; 0.26±0.09 and 0.27±0.01 on July 9, 2004, July 18, 2004 and June 19, 2005. At the Llano de los Juanes research site on these dates, B is 0.25, 0.26 and 0.24.

It is important to mention that $NEF_{S\text{-}SEBIt}$ and NEF_{Seguin} are very similar, but an offset equivalent to the NEF for water (lake at the middle of the greenhouse area) is observed for $NEF_{S\text{-}SEBIt}$ suggesting a low wet edge, which would be easy to recalibrate. The fact that $R^2 > 0.96$ and the slope between $NEF_{S\text{-}SEBIt}$ and NEF_{Seguin} is close to 1 on the three dates is very important, as these two models are calculated with very different approaches and $NEF_{S\text{-}SEBIt}$ requires fewer input variables than NEF_{Seguin}.

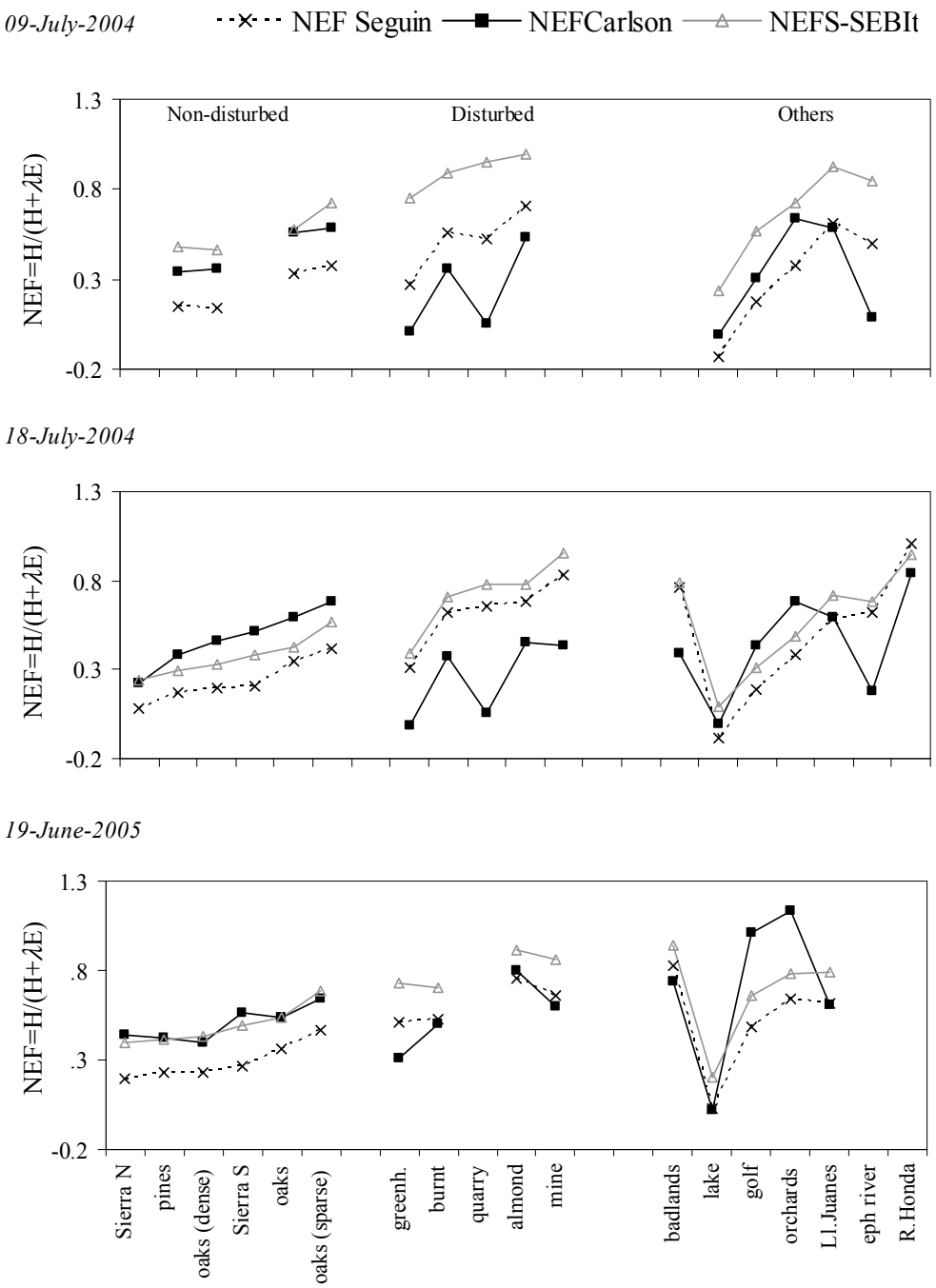

Figure 4. NEF (non-evaporative fraction) over selected surface types calculated by the NEF_{Seguin}, $NEF_{Carlson}$ and $NEF_{S\text{-}SEBIt}$ models. The first set of surfaces corresponds to undisturbed sites. Sierra N and Sierra S are pine forests on the northern and southern slopes of the Sierra Nevada Mountains, three densities of oak relicts correspond to: oaks (dense), oaks (sparse) and oaks. Pines correspond old reforested sites. The second set is for disturbed sites: greenhouses (Greenh), a strong burn scar (burnt), a limestone quarry (quarry), almond orchards (almond), and an abandoned mine (mine). The third set comprises miscellaneous sites: the Tabernas badlands, a lake, a golf coarse (golf), irrigated citrus orchards along the Andarax River (orchards); Ll. Juanes is the *Llano de los Juanes*, eph.river is the ephemeral Andarax River and R.Honda is the *Rambla Honda* research site.

4.2 Field validation of the non-evaporative fraction models

Air temperature

Air temperature was required to estimate longwave incoming radiation, sensible heat flux and the S-SEBI$_t$ evaporative fraction (Table 2).

The overall adjustment is good (< 2ºC), but T_{air} estimates are subject to local errors. Altitude is not the only factor affecting T_{air}, but using this approach has the advantage of not having to use meteorological station data. Also, any systematic error in T_s retrieval will propagate in T_{air}. These errors should therefore be compensated when calculating T_s-T_{air} differences for estimating sensible heat flux. In our case, this approach yields better results than the [3] wet and dry pixel method.

Table 2. Air temperature estimates at the study site. Mean Absolute Error (MAE) is the average absolute difference in residuals between estimated and measured air temperature at the meteorological stations. MAE after adjustment is the temperature corrected for a lapse rate of 6.5ºC per 1000 m. Reference altitude is the altitude of the pixels the apex temperature was taken from.

	July 18, 2004 n=11	**July 7, 2004** n=10	**July 19, 2004** n=12
R^2 (observed-predicted)	0.61	0.74	0.67
MAE before adjustment (ºC)	4.31	3.40	2.68
MAE after adjustment (ºC)	1.96	2.07	1.93
T apex (ºC)	24.0	24.61	23.39
Reference altitude (m)	1800	1833	1099

Daily net radiation (Rnd)

Results from estimating the Rnd using ASTER data show very good agreement with field data (Table 3), with an overall error < 5% of Rnd and close to the 1:1 line. Reported Rnd accuracy of the net radiometer is around ±10% (NR-lite by Kipp&Zonen), which is the case for some remote sensing studies [2]. Other remote sensing studies have reported an Rnd RMSE of 20-30 Wm^{-2} [57-59] or 40-50 Wm^{-2} [47,60,61] depending on data, model and surface type used for validation.

Emissivity values estimated in this work are reasonable according to reported values for soil and vegetation [35, 62] The emissivity values used in the van de Griend and Owe [35, 62] model were 0.91 for bare soil, between 0.94-0.97 for shrubs and grasslands with partial cover depending on vegetation type, and 0.98-0.99 for complete vegetation cover. At the Rambla Honda field site measured emissivity is highly variable, between 0.94-0.97 for soil and 0.94-0.97 for vegetation ([22]). Given the pixel size (90 m) the mix of soil and vegetation makes it very difficult to get pure pixels. In this area, estimated emissivity using Aster data ranged between a minimum of 0.91 up to a maximum of 0.95 depending on vegetation type and cover.

In the whole study region, maximum emissivity correspond to sites with complete cover such as forests, golf course, and irrigated orchards (0.97-0.98 depending on date). Estimated emissivity decreases with vegetation cover reaching values of 0.92-0.94 at the shrublands in Sierra de Gádor. The lowest emissivity values correspond to almond orchards dominated by bare soil signature (0.94-0.92), limestone quarry and mining areas (0.90-0.92).

Table 3. Daily Net Radiation Rnd (Wm^{-2}) of *Retama, Anthyllis, Stipa*, shrubs, and bare soil at the *Llano de los Juanes* and *Rambla Honda* research sites. "Field" is the Rnd field measurement, and ASTER is the Rnd estimated using ASTER and ancillary data. AE is the absolute value of (Rnd_{field}-Rnd_{Aster}). The % Error is calculated as (Rnd_{field}-Rnd_{Aster})100/ Rnd_{field}. For an overall error evaluation, the MAE (mean absolute error), the average AE, the mean % error, (% Error), R^2 (Pearson correlation coefficient), p (probability), slope and regression intercept between field and ASTER results were calculated.

Date	Surface type	Location	Field Rnd (Wm^{-2})	ASTER Rnd (Wm^{-2})	AE (Wm^{-2})	% Error
09-07-04	Shrubs	Llano Juanes	188.70	184.21	4.49	1.30
18-07-04	Shrubs	Llano Juanes	179.71	189.70	9.99	5.30
19-06-05	Shrubs	Llano Juanes	183.40	192.40	9.00	4.90
18-07-04	*Retama*	Rambla Honda	166.53	152.53	14.00	-8.41
18-07-04	*Anthyllis*	Rambla Honda	165.07	156.59	8.48	-5.14
18-07-04	*Stipa*	Rambla Honda	159.28	155.97	3.31	-2.08
18-07-04	Bare soil	Rambla Honda	112.68	110.19	2.49	-2.21
	MAE		7.39			
	RMSE		8.94			
	Mean % error		4.38			
	R^2		0.91			
	p		0.0008			
	slope		1.09			
	intercept		-16.14			

Sensible heat flux (H) and the non-evaporative fraction (NEF)

The non-evaporative fraction (NEF) and the sensible heat flux H were validated using Eddy Covariance data at the *Llano de los Juanes* research site and a SVAT model previously calibrated with the Eddy Covariance and Bowen Ratio systems at the *Rambla Honda* research site (Figure 1). A lake located at the greenhouse area was considered to evaporate at potential rate (H~0).

Validation results are similar for NEF and H (Wm^{-2}) (Tables 4 and 5). H_{Seguin} and therefore, NEF_{Seguin}, provide the best overall performance being closer to the 1:1 line. Although the R^2 is higher for $H_{Carlson}$ and therefore, so is $NEF_{Carlson}$, their RMSE is still the highest of the three models.

At the *Llano de los Juanes* research site, ASTER results underestimate H compared to Eddy Covariance measurements using H_{Seguin} and $H_{Carlson}$ around 30%. In addition to the simplicity of the modeling approaches, there is an error propagation from input data. Thus, although reported errors in T_s are within acceptable quality levels (< 4 K) they contribute to final error combined with the error in T_{air} estimates (< 2 K) and in the aerodynamic resistance that, in this case, is probably too high.

We should also be aware that the Eddy Covariance and Bowen Ratio techniques are subject to error. Uncertainty levels in the Eddy Covariance are around 20% [63] and 10% in the Bowen Ratio technique [64, 65]. Moreover, in semi-arid areas with sparse vegetation cover, error in energy fluxes tends to be even higher, around 25% [25].

Daily H estimates from remote sensing models usually contribute the highest uncertainty to the surface energy balance, with errors at a daily scale of around 20-30% or 1 mm day^{-1}, equivalent to ~29 Wm^{-2} [2]. In our case, the RMSEs for H_{Seguin} and $H_{S\text{-}SEBIt}$, are below that threshold, but not for

$H_{Carlson,}$ Individual errors range between 3% and 30% for the worst cases (*Llano de los Juanes* and $H_{Carlson}$) being the lowest in general for $H_{S\text{-}SEBIt}$.

In general, reported range of errors in H varies widely depending on surface type, image data, time average period, and model used. [66] consider an error of around 50 Wm^{-2} as acceptable for instantaneous H and 23 Wm^{-2} for daily H. In the literature, best case errors for instantaneous (half-hourly) and daily fluxes are around 10-22 Wm^{-2} [2, 57] and can reach up to 50%, even using sophisticated models when parameterization is not good. It is more complicated to get good estimates over heterogeneous semiarid areas than over agricultural or humid sites [67]. [68] obtained an RMSE of 43.35 Wm^{-2} for instantaneous H, while [69] found errors of around 40% in the Great Basin Desert, and [70] obtained an RMSE=47 Wm^{-2} for instantaneous H using dual angle observations over a semiarid grassland in Mexico.

Our results for the NEF (non-evaporative fraction) are within errors reported for evaporative fraction at a daily scale from the SEBAL model, with a more complex parameterization, with RMSEs in the daily evaporative fraction (EF=1-NEF) between 0.10-0.20 [71]. [72] obtained an RMSE for daily EF of 0.13, and [45] between 0.09-0.05 using S-SEBIt over European forests compared to Euroflux data.

Results from field validation confirm previous results about model performance for selected surface types as shown in Figures 3 and 4. Given the simplicity of the models used in this study, our results are reasonable, being the errors within ranges reported in the literature.

Table 4. Field validation of the daily sensible heat flux (H) in Wm^{-2} estimated by the H_{Seguin}, $H_{Carlson}$ and $H_{S\text{-}SEBIt}$ models. AE is the absolute error (absolute difference between model and field observations). For overall error evaluation, the MAE (mean absolute error), which is the average AE, the R^2 (Pearson correlation coefficient), p (probability), slope and intercept of the regression between field and ASTER were calculated.

Date	Surface type	Location	Field	Seguin		Carlson		S-SEBI*t*	
			H (Wm^{-2})	H (Wm^{-2})	AE (Wm^{-2})	H (Wm^{-2})	AE (Wm^{-2})	H (Wm^{-2})	AE (Wm^{-2})
09-07-04	Shrubs	Llano Juanes	158.77	110.29	48.48	107.69	51.07	169.48	10.71
18-09-04	Shrubs	Llano Juanes	154.94	106.70	48.24	107.58	47.36	130.40	24.54
19-06-05	Shrubs	Llano Juanes	157.43	115.99	41.44	114.42	43.01	150.19	7.24
18-09-04	*Retama*	Rambla Honda	157.34	152.39	4.95	109.56	47.78	143.78	13.55
18-09-04	*Anthyllis*	Rambla Honda	133.15	139.38	6.24	80.56	52.59	139.06	5.91
18-09-04	*Stipa*	Rambla Honda	122.54	126.16	3.62	106.29	16.24	124.75	2.21
09-07-04	lake	Greenhouses	0.00	-27.33	27.33	-0.93	0.93	46.61	46.61
18-09-04	lake	Greenhouses	0.00	-19.07	19.07	-1.34	1.34	21.54	21.54
19-06-05	lake	Greenhouses	0.00	7.06	7.06	5.01	5.01	49.41	49.41
	MAE				22.94		29.48		20.19
	RMSE				29.12		36.58		25.97
	R^2				0.900		0.97		0.948
	p				0.00009		0.000001		0.00001
	slope				0.904		0.694		0.702
	intercept				-9.833		1.66		39.304

Table 5. Field validation of the NEF (non-evaporative fraction), NEF=H/(H+λE) NEF_{Seguin}, $NEF_{Carlson}$ and $NEF_{S\text{-}SEBIt}$ models. AE is the absolute error (absolute difference between model and field observations). When using the lake for validation, two cases have been considered G_{lake}=50 Wm^{-2} and G_{lake}=-50 Wm^{-2} . For an overall error evaluation, the MAE (mean absolute error), which is the average AE, the R^2 (Pearson correlation coefficient), p (probability), slope and regression intercept between field and ASTER data were calculated (n=9 observations). For NEF_{Seguin} and $NEF_{Carlson}$ overall error estimation has been performed twice, one with the dataset including the lake when G_{lake}=-50 Wm^{-2} and another with the dataset including the lake when G_{lake}= -50 Wm^{-2} , the latter in parenthesis the table.

Date	Surface	Location	Field	Seguin		Carlson		S-SEBI*t*	
			NEF	NEF	AE	NEF	AE	NEF	AE
09-07-04	Shrubs	Llano Juanes	0.88	0.61	0.27	0.59	0.29	0.93	0.05
18-07-04	Shrubs	Llano Juanes	0.92	0.59	0.33	0.61	0.31	0.72	0.2
19-06-05	Shrubs	Llano Juanes	0.88	0.62	0.26	0.61	0.27	0.79	0.09
18-07-04	*Retama*	Rambla Honda	0.97	1.00	0.03	0.72	0.25	0.94	0.03
18-07-04	*Anthyllis*	Rambla Honda	0.83	0.89	0.06	0.51	0.32	0.89	0.06
18-07-04	*Stipa*	Rambla Honda	0.79	0.81	0.02	0.68	0.11	0.8	0.01
09-07-04	Lake $_{(G=50)}$	Greenhouses	0.00	-0.17	0.17	-0.01	0.01	0.24	0.24
09-07-04	Lake $_{(G=-50)}$	Greenhouses		-0.11	0.11	0.00	0.00		
18-07-04	Lake $_{(G=50)}$	Greenhouses	0.00	-0.12	0.12	-0.01	0.01	0.10	0.10
18-07-04	Lake $_{(G=-50)}$	Greenhouses		-0.07	0.07	-0.01	0.01		
19-06-05	Lake $_{(G=50)}$	Greenhouses	0.00	0.04	0.04	0.03	0.03	0.21	0.21
19-06-05	Lake $_{(G=-50)}$	Greenhouses		0.02	0.02	0.02	0.02		
MAE $_{Glake=50\ (-50)}$				0.14 (0.13)		0.18 (0.17)		0.11	
RMSE $_{Glake=50\ (-50)}$				0.18 (0.17)		0.22 (0.22)		0.13	
R^2 $_{Glake=50\ (-50)}$				0.88 (0.89)		0.97 (0.97)		0.94	
p $_{Glake=50\ (-50)}$				0.0002 (0.0002)		0.000002 (0.000000)		0.00001	
Slope $_{Glake=50\ (-50)}$				0.94 (0.91)		0.70 (0.70)		0.75	
Intercept $_{Glake=50\ (-50)}$				-0.08 (-0.05)		0.01 (0.00)		0.18	

5. Conclusions

Three operative models for estimating the non-evaporative fraction (NEF) as an indicator of the surface water deficit, were evaluated in a semiarid area of southeast Spain. Of the three models evaluated, the NEF computed with the Simplified Relationship for unstable conditions [8] was found to be equivalent to NEF estimated from S-SEBIt (Simplified-Surface Energy Balance Index) [4] modified in our study to account for varying atmospheric conditions (R^2>0.97, p<0.0001). This is important, as the two algorithms are very different. One explicitly solves the variables in the surface energy balance, while the other uses a contextual relationship between albedo and surface temperature requiring fewer input variables. On the other hand, the spatial patterns obtained with Carlson's model [9] were different from the other two models.

Comparison to field data showed that net radiation (Rn) modeled with ASTER data produces very good results (R^2=0.91, p<0.0001), with an overall error within reported instrumental accuracy

(< 5%). Validation of sensible heat flux (H) and NEF showed the most coherent spatial patterns with Seguin's approach [8] followed by the S-SEBI$_t$ model. Of the three models, Carlson´s approach had the highest RMSE. In semiarid sites with low NDVI, estimating the B exchange coefficient for sensible heat transfer based solely on NDVI produces unrealistic patterns, making it preferable to use a constant value of B, at least as a first approximation.

The errors found for NEF_{Seguin} and $NEF_{S\text{-}SEBIt}$ are within those reported in the literature (RMSE for NEF are ~ 0.18 and 0.13 and for H are 29.12 Wm^{-2} and 25.97 Wm^{-2} for Seguin's and S-SEBI$_t$ respectively). Given the simplicity of the models used, these results are very promising for operative monitoring of the surface water deficit and the partition of surface energy into sensible and latent heat flux.

Acknowledgements

This study received financial support from several different research projects: the integrated EU project, DeSurvey (A Surveillance System for Assessing and Monitoring of Desertification) (ref.: FP6-00.950, Contract nº. 003950), the PROBASE (ref.: CGL2006-11619/HID) and CANOA (ref.: CGL2004-04919-C02-01/HID) projects funded by the Spanish Ministry of Education and Science; and the BACAEMA ('Balance de carbono y de agua en ecosistemas de matorral mediterráneo en Andalucía: Efecto del cambio climático', RNM-332) and CAMBIO ('Efectos del cambio global sobre la biodiversidad y el funcionamiento ecosistémico mediante la identificación de áreas sensibles y de referencia en el SE ibérico', RNM 1280) projects funded by the Junta de Andalucía (Andalusian Regional Government). The authors wish to thank Ana M. Were and Angeles Ruiz for their helpful comments, S.Vidal and R.Ordiales for IT assistance, and Deborah Fuldauer for correcting and improving the English of the text. We thank two anonymous reviewers for improving this manuscript.

References

1. Wilson, K. B.; Baldocchi, D. D.; Aubinet, M.; Berbigier, P.; Bernhofer, C.; Dolman, H.; Falge, E.; Field, C.; Goldstein, A.; Granier, A.; Grelle, A.; Halldor, T.; Hollinger, D.; Katul, G.; Law, B. E.; Lindroth, A.; Meyers, T.; Moncrieff, J.; Monson, R.; Oechel, W.; Tenhunen, J.; Valentini, R.; Verma, S.; Vesala, T.; Wofsy, S. Energy Partitioning Between Latent and Sensible Heat Flux During the Warm Season at FLUXNET Sites. *Water Resour. Res.* **2002,** *38*.
2. Kustas, W. P.; Norman, J. M. Use of Remote Sensing for Evapotranspiration Monitoring Over Land Surfaces. *Hydrol. Sci. J.* **1996,** *41,* 495-516.
3. Bastiaanssen, W. G. M.; Menenti, M.; Feddes, R. A.; Holtslag, A. A. M. A Remote Sensing Surface Energy Balance Algorithm for Land (SEBAL) - 1. Formulation. *J. Hydrol.* **1998,** *213,* 198-212.
4. Roerink, G. J.; Su, Z.; Menenti, M. S-SEBI: A Simple Remote Sensing Algorithm to Estimate the Surface Energy Balance. *Phys. Chem. Earth Pt. B.* **2000,** *25,* 147-157.
5. Domingo, F.; Villagarcía, L.; Boer, M. M.; Alados-Arboledas, L.; Puigdefábregas, J. Evaluating the Long-Term Water Balance of Arid Zone Stream Bed Vegetation Using Evapotranspiration Modelling and Hillslope Runoff Measurements. *J. Hydrol.* **2001,** *243,* 17-30.

6. Moran, M. S.; Kustas, W. P.; Vidal, A.; Stannard, D. I.; Blanford, J. H.; Nichols, W. D. Use of Ground-Based Remotely-Sensed Data for Surface-Energy Balance Evaluation of A Semiarid Rangeland. *Water Resour. Res.* **1994,** *30,* 1339-1349.
7. Jackson, R. D.; Reginato, R. J.; Idso, S. B. Wheat Canopy Temperature - Practical Tool for Evaluating Water Requirements. *Water Resour. Res.* **1977,** *13,* 651-656.
8. Seguin, B.; Itier, B. Using Midday Surface-Temperature to Estimate Daily Evaporation From Satellite Thermal Ir Data. *Int. J. Remote Sens.* **1983,** *4,* 371-383.
9. Carlson, T. N.; Capehart, W. J.; Gillies, R. R. A New Look at the Simplified Method for Remote-Sensing of Daily Evapotranspiration. *Remote Sens. Environ.* **1995,** *54,* 161-167.
10. Pulido-Bosch, A.; Pulido-Leboeuf, P.; Molina-Sánchez, L.; Vallejos, A.; Martín-Rosales, W. Intensive Agriculture, Wetlands, Quarries and Water Management. A Case Study (Campo de Dalias, SE Spain). *Environ. Geol.* **2000,** *40,* 163-168.
11. French, A. N.; Jacob, F.; Anderson, M. C.; Kustas, W. P.; Timmermans, W.; Gieske, A.; Su, Z.; Su, H.; Mccabe, M. F.; Li, F.; Prueger, J.; Brunsell, N. Surface Energy Fluxes With the Advanced Spaceborne Thermal Emission and Reflection Radiometer (ASTER) at the Iowa 2002 SMACEX Site (USA). *Remote Sens. Environ.* **2005,** *99,* 55-65.
12. Jacob, F.; Petitcolin, F.; Schmugge, T.; Vermote, E.; French, A.; Ogawa, K. Comparison of Land Surface Emissivity and Radiometric Temperature Derived From MODIS and ASTER Sensors. *Remote Sens. Environ.* **2004,** *90,* 137-152.
13. López-Bermúdez; F.; Boix-Fayos; C.; Solé-Benet; A.; Albaladejo; J.; Barberá; G.C.; del Barrio; G.; Castillo; V.; García; J.; Lázaro; R.; Martínez-Mena; M.D.; Mosch; W.; Navarro-Cano; J.A.; Puigdefábregas; J.; Sanjuán; M. *Landscapes and Desertification in South-East Spain: Overview and Field Sites. Field Trip Guide. A-5*. 6th International conference on Geomorphology. Sociedad Española de Geomorfología. 2005, pp 40.
14. Oyonarte, C.; Perez- Pujalte, A.; Delgado, G.; Delgado, R.; Almendros, G. Factors Affecting Soil Organic-Matter Turnover in A Mediterranean Ecosystems From Sierra De Gador (Spain) - An Analytical Approach. *Soil Sci. Plan.* **1994,** *25,* 1929-1945.
15. Contreras, S. Spatial *Distribution of the Annual Water Balance in Semi-Arid Mountainous Regions: Application to Sierra de Gádor (Almería, SE Spain)*. Ph.D thesis (in spanish). Depto de Hidrogeología y Química Analítica. Universidad de Almería. 2006; pp 41-69
16. Li; X. Y.; Contreras; S.; Solé-Benet A. Spatial Distribution of Rock Fragments in Dolines: a Case Study in a Semiarid Mediterranean Mountain-Range (Sierra Gádor , SE Spain). *Catena* **2007**, in press.
17. Puigdefábregas; J.; Delgado; L.; Domingo; F.; Cueto; M.; Gutiérrez; L.; Lázaro; R.; Nicolau; J.M.; Sánchez; G.; Solé-Benet; A.; Vidal; S.; Aguilera; C.; Brenner; A.; Clark; S.; Incoll; L. In *Mediterranean Desertification and Land Use*; Brandt, J.; Thornes, J., Eds.; John Wiley & Sons, Ltd., 1996; pp 137-168.
18. Puigdefábregas, J.; Sole, A.; Gutierrez, L.; del Barrio, G.; Boer, M. Scales and Processes of Water and Sediment Redistribution in Drylands: Results From the Rambla Honda Field Site in Southeast Spain. *Earth-Sci. Rev.* **1999,** *48,* 39-70.
19. Puigdefábregas, J. The Role of Vegetation Patterns in Structuring Runoff and Sediment Fluxes in Drylands. *Earth Surf. Proc. Land.* **2005,** *30,* 133-147.

20. Domingo, F.; Villagarcía, L.; Brenner, A. J.; Puigdefábregas, J. Evapotranspiration Model for Semi-Arid Shrub-Lands Tested Against Data From SE Spain. *Agric. For. Meteorol.* **1999,** *95,* 67-84.
21. Domingo, F.; Brenner, A. J.; Gutierrez, L.; Clark, S. C.; Incoll, L. D.; Aguilera, C. Water Relations Only Partly Explain the Distributions of Three Perennial Plant Species in a Semi-Arid Environment. *Biol. Plantarum* **2003,** *46,* 257-262.
22. Domingo, F.; Villagarcía, L.; Brenner, A. J.; Puigdefábregas, J. Measuring and Modelling the Radiation Balance of a Heterogeneous Shrubland. *Plant Cell Environ.* **2000,** *23,* 27-38.
23. Domingo, F.; Villagarcía, L.; Boer, M. M.; Alados-Arboledas, L.; Puigdefábregas, J. Evaluating the Long-Term Water Balance of Arid Zone Stream Bed Vegetation Using Evapotranspiration Modelling and Hillslope Runoff Measurements. *J. Hydrol.* **2001,** *243,* 17-30.
24. Domingo, F.; Gutierrez, L.; Brenner, A. J.; Aguilera, C. Limitation to Carbon Assimilation of Two Perennial Species in Semi-Arid South-East Spain. *Biol. Plantarum* **2002,** *45,* 213-220.
25. Were, A.; Villagarcía, L.; Domingo, F.; Alados-Arboledas, L.; Puigdefábregas, J. Analysis of Effective Resistance Calculation Methods and Their Effect on Modelling Evapotranspiration in Two Different Patches of Vegetation in Semi-Arid SE Spain. *HESSD.* **2007**, 4, 1-44.
26. Hasse, P.; Pugnaire, F. I.; Clark, S. C.; Incoll, L. D. Photosynthetic Rate and Canopy Development in the Drought-Deciduous Shrub *Anthyllis Cytisoides* L. *J. Arid Environ*. **2000,** *46,* 79-91.
27. Moro, M. J.; Pugnaire, F. I.; Haase, P.; Puigdefábregas, J. Mechanisms of Interaction Between a Leguminous Shrub and Its Understorey in a Semi-Arid Environment. *Ecography* **1997,** *20,* 175-184.
28. Pugnaire, F. I.; Haase, P.; Puigdefábregas, J.; Cueto, M.; Clark, S. C.; Incoll, L. D. Facilitation and Succession Under the Canopy of a Leguminous Shrub, *Retama Sphaerocarpa*, in a Semi-Arid Environment in South-East Spain. *Oikos* **1996,** *76,* 455-464.
29. Brenner, A. J.; Incoll, L. D. The Effect of Clumping and Stomatal Response on Evaporation From Sparsely Vegetated Shrublands. *Agric. For. Meteorol.* **1997,** *84,* 187-205.
30. Shuttleworth, W. J.; Wallace, J. S. Evaporation From Sparse Crops - An Energy Combination Theory. *Q. J. Roy.Meteor. Soc*. **1985,** *111,* 839-855.
31. Dolman, A. J. A Multiple-Source Land-Surface Energy-Balance Model for Use in General-Circulation Models. *Agric. For. Meteorol.* **1993,** *65,* 21-45.
32. http://asterweb.jpl.nasa.gov/
33. Fu, P. D.; Rich, P. M. A Geometric Solar Radiation Model With Applications in Agriculture and Forestry. *Comput. Electron. Agr.* **2002,** *37,* 25-35.
34. Liang, S. L. Narrowband to Broadband Conversions of Land Surface Albedo I Algorithms. *Remote Sens. Environ.* **2001,** *76,* 213-238.
35. Van de Griend, A. A.; Owe, M. On the Relationship Between Thermal Emissivity and the Normalized Difference Vegetation Index for Natural Surfaces. *Int. J. Remote Sens.* **1993,** *14,* 1119-1131.
36. Idso, S. B.; Jackson, R. D. Thermal Radiation From Atmosphere. *J. Geophys. Res.* **1969,** *74,* 5397-5403.
37. Brutsaert, W. *Evaporation into the Atmosphere. Theory, History, and Applications;* Dordrecht: Holland, D. Reidel Publishing Company, 1982; pp 293.

38. Jackson, R. D.; Moran, M. S.; Gay, L. W.; Raymond, L. H. Evaluating Evaporation From Field Crops Using Airborne Radiometry and Ground-Based Meteorological Data. *Irrigation Sci.* **1987,** *8,* 81-90.
39. Kustas, W. P.; Perry, E. M.; Doraiswamy, P. C.; Moran, M. S. Using Satellite Remote-Sensing to Extrapolate Evapotranspiration Estimates in Time and Space Over A Semiarid Rangeland Basin. *Remote Sens. Environ.* **1994,** *49,* 275-286.
40. Hall, F. G.; Huemmrich, K. F.; Goetz, S. J.; Sellers, P. J.; Nickeson, J. E. Satellite Remote-Sensing of Surface-Energy Balance - Success, Failures, and Unresolved Issues in Fife. *J. Geophys. Res.-Atmos***. 1992,** *97,* 19061-19089.
41. Caselles, V.; Artigao, M. M.; Hurtado, E.; Coll, C.; Brasa, A. Mapping Actual Evapotranspiration by Combining Landsat TM and NOAA-AVHRR Images: Application to the Barrax Area, Albacete, Spain. *Remote Sens. Environ.* **1998,** *63,* 1-10.
42. Sugita, M.; Brutsaert, W. Daily Evaporation Over A Region From Lower Boundary-Layer Profiles Measured With Radiosondes. *Water Resour. Res.* **1991,** *27,* 747-752.
43. Prihodko, L.; Goward, S. N. Estimation of Air Temperature From Remotely Sensed Surface Observations. *Remote Sens. Environ.* **1997,** *60,* 335-346.
44. Czajkowski, K. P.; Goward, S. N.; Mulhern, T.; Goetz, S. J.; Walz, A.; Shirey, D.; Stadler, S.; Prince, S. D.; Dubayah, R. O. In *Thermal remote sensing in land surface processes*; Quattrochi, D.A.; Luvall, J. C., Eds.; Boca Raton, Florida: CRC Press, 2000; pp 11-32.
45. Verstraeten, W. W.; Veroustraete, F.; Feyen, J. Estimating Evapotranspiration of European Forests From NOAA-Imagery at Satellite Overpass Time: Towards an Operational Processing Chain for Integrated Optical and Thermal Sensor Data Products. *Remote Sens. Environ.* **2005,** *96,* 256-276.
46. Sobrino, J. A.; Gomez, M.; Jimenez-Munoz, J. C.; Olioso, A.; Chehbouni, G. A Simple Algorithm to Estimate Evapotranspiration From DAIS Data: Application to the DAISEX Campaigns. *J. Hydrol.* **2005,** *315,* 117-125.
47. Gómez, M.; Olioso, A.; Sobrino, J. A.; Jacob, F. Retrieval of Evapotranspiration Over the Alpilles/ReSeDA Experimental Site Using Airborne POLDER Sensor and a Thermal Camera. *Remote Sens. Environ.* **2005,** *96,* 399-408.
48. Koenker, R.; Hallock, K. F. Quantile Regression. *J. Econ. Perspect.* **2001,** *15,* 143-156.
49. Villagarcía; L.; Domingo; F.; Alados-Arboledas; L.; Puigdefábregas; J. Modelización de la evapotranspiración real en rodales de tres especies vegetales del SE Español. *V Simposio sobre el agua en Andalucía*. Editorial de la Universidad de Almería, Almería, 2001, 1, 107-118.
50. Paracuellos, M. How Can Habitat Selection Affect the Use of a Wetland Complex by Waterbirds? *Biodivers. Conserv.* **2006,** *15,* 4569-4582.
51. Oswald, C. J.; Rouse, W. R. Thermal Characteristics and Energy Balance of Various-Size Canadian Shield Lakes in the Mackenzie River Basin. *J. Hydrometeorol***. 2004,** *5,* 129-144.
52. Burba, G. G.; Verma, S. B.; Kim, J. Surface Energy Fluxes of *Phragmites Australis* in a Prairie Wetland. *Agric. For. Meteorol.* **1999,** *94,* 31-51.
53. Rodríguez-Rodríguez, M.; Moreno-Ostos, E. Heat Budget, Energy Storage and Hydrological Regime in a Coastal Lagoon. *Limnologica* **2006,** *36,* 217-227.

54. Sánchez-Carrillo, S.; Angeler, D. G.; Sanchez-Andres, R.; Alvarez-Cobelas, M.; Garatuza-Payan, J. Evapotranspiration in Semi-Arid Wetlands: Relationships Between Inundation and the Macrophyte-Cover: Open-Water Ratio. *Adv. Water Resour.* **2004,** *27,* 643-655.
55. Burba, G. G.; Verma, S. B.; Kim, J. Energy Fluxes of an Open Water Area in a Mid-Latitude Prairie Wetland. *Bound-Lay. Meteorol.* **1999,** *91,* 495-504.
56. Nosetto, M. D.; Jobbagy, E. G.; Paruelo, J. M. Land-Use Change and Water Losses: the Case of Grassland Afforestation Across a Soil Textural Gradient in Central Argentina. *Glob. Change Biol.* **2005,** *11,* 1101-1117.
57. Su, Z. The Surface Energy Balance System (SEBS) for Estimation of Turbulent Heat Fluxes. *Hydrol. Earth Syst. Sc. s* **2002,** *6,* 85-99.
58. Jacob, F.; Olioso, A.; Gu, X. F.; Su, Z. B.; Seguin, B. Mapping Surface Fluxes Using Airborne Visible, Near Infrared, Thermal Infrared Remote Sensing Data and a Spatialized Surface Energy Balance Model. *Agronomie* **2002,** *22,* 669-680.
59. Batra, N.; Islam, S.; Venturini, V.; Bisht, G.; Jiang, J. Estimation and Comparison of Evapotranspiration From MODIS and AVHRR Sensors for Clear Sky Days Over the Southern Great Plains. *Remote Sens. Environ.* **2006,** *103,* 1-15.
60. Timmermans, W. J.; Kustas, W. P.; Anderson, M. C.; French, A. N. An Intercomparison of the Surface Energy Balance Algorithm for Land (SEBAL) and the Two-Source Energy Balance (TSEB) Modeling Schemes. *Remote Sens. Environ. In Press, Corrected Proof.*
61. Bisht, G.; Venturini, V.; Islam, S.; Jiang, L. Estimation of the Net Radiation Using MODIS (Moderate Resolution Imaging Spectroradiometer) Data for Clear Sky Days. *Remote Sens. Environ.* **2005,** *97,* 52-67.
62. Rubio, E.; Caselles, V.; Badenas, C. Emissivity Measurements of Several Soils and Vegetation Types in the 8-14 Mu m Wave Band: Analysis of Two Field Methods. *Remote Sens. Environ.* **1997,** *59,* 490-521.
63. Baldocchi, D.; Falge, E.; Gu, L. H.; Olson, R.; Hollinger, D.; Running, S.; Anthoni, P.; Bernhofer, C.; Davis, K.; Evans, R.; Fuentes, J.; Goldstein, A.; Katul, G.; Law, B.; Lee, X. H.; Malhi, Y.; Meyers, T.; Munger, W.; Oechel, W.; U, K. T. P.; Pilegaard, K.; Schmid, H. P.; Valentini, R.; Verma, S.; Vesala, T.; Wilson, K.; Wofsy, S. FLUXNET: A New Tool to Study the Temporal and Spatial Variability of Ecosystem-Scale Carbon Dioxide, Water Vapor, and Energy Flux Densities. *B. Am. Meteorol. Soc.* **2001,** *82,* 2415-2434.
64. Nie, D.; Flitcroft, I. D.; Kanemasu, E. T. Performance of Bowen-Ratio Systems on A Slope. *Agric. For. Meteorol.* **1992,** *59,* 165-181.
65. Gurney, R. J.; Sewell, I. J. In *Scaling-up: from cell to landscape;* P. R. Van Gardingen, G. M.; Foody; Curran, P. J., Eds.; Cambridge University Press, Cambridge, UK, 1997; pp 319-346.
66. Seguin, B.; Becker, F.; Phulpin, T.; Gu, X. F.; Guyot, G.; Kerr, Y.; King, C.; Lagouarde, J. P.; Ottle, C.; Stoll, M. P.; Tabbagh, A.; Vidal, A. IRSUTE: A Minisatellite Project for Land Surface Heat Flux Estimation From Field to Regional Scale. *Remote Sens. Environ.* **1999,** *68,* 357-369.
67. Wassenaar, T.; Olioso, A.; Hasager, C.; Jacob, F.; Chehbouni, A. In *Recent Advances in Quantitative Remote Sensing*; Sobrino, J. A., Ed.; Universidad de Valencia. 2002; pp 319-328.

68. Humes, K.; Hardy, R.; Kustas, W.; Prueger, J.; Starks. P. In *Thermal remote sensing in land surface processes*; Quattrochi, D.A.; Luvall, J. C., Eds.; Boca Raton, Florida: CRC Press, 2000; pp 110-132.
69. Laymon, C. A.; Qattrochi, D. A. In *Thermal remote sensing in land surface processes*; Quattrochi, D.A.; Luvall, J. C., Eds.; Boca Raton, Florida: CRC Press, 2000; pp 133-159.
70. Chehbouni, A.; Nouvellon, Y.; Lhomme, J. P.; Watts, C.; Boulet, G.; Kerr, Y. H.; Moran, M. S.; Goodrich, D. C. Estimation of Surface Sensible Heat Flux Using Dual Angle Observations of Radiative Surface Temperature. *Agric. For. Meteorol.* **2001,** *108,* 55-65.
71. Bastiaanssen, W. G. M.; Pelgrum, H.; Wang, J.; Ma, Y.; Moreno, J. F.; Roerink, G. J.; van der Wal, T. A Remote Sensing Surface Energy Balance Algorithm for Land (SEBAL) - 2. Validation. *J. Hydrol.* **1998,** *213,* 213-229.
72. Jiang, L.; Islam, S. Estimation of Surface Evaporation Map Over Southern Great Plains Using Remote Sensing Data. *Water Resour. Res.* **2001,** *37,* 329-340.